Observation of a Core-Diffracted P-Wave From a Farside Impact With Implications for the Lower-Mantle Structure of Mars

Author(s):
Duran, Andrea Cecilia; Khan, Amir; Ceylan, Savas; Charalambous, Constantinos; Kim, Doyeon; Drilleau, Mélanie; Samuel, Henri; Giardini, Domenico

Publication date:
2022-11-16

Permanent link:
https://doi.org/https://doi.org/10.3929/ethz-b-000582973

Originally published in:
Geophysical Research Letters 49(21), https://doi.org/10.1029/2022GL100887

Geophysical Research Letters

RESEARCH LETTER
10.1029/2022GL100887

Observation of a Core-Diffracted P-Wave From a Farside Impact With Implications for the Lower-Mantle Structure of Mars

C. Durán[1], A. Khan[1,2], S. Ceylan[1], C. Charalambous[3], D. Kim[1], M. Drilleau[4], H. Samuel[5], and D. Giardini[1]

[1]Institute of Geophysics, ETH Zürich, Zürich, Switzerland, [2]Physik-Institut, University of Zürich, Zürich, Switzerland, [3]Department of Electrical and Electronic Engineering, Imperial College London, London, UK, [4]Institut Supérieur de l'Aéronautique et de l'Espace ISAE-SUPAERO, Toulouse, France, [5]Institut de Physique du Globe de Paris, CNRS, Université de Paris, Paris, France

Key Points:

- We have identified a core-diffracted wave from a farside impact
- We infer the lower mantle P-wave velocity structure hitherto unconstrained
- We find indications for a lower mantle structure that appears to be incompatible with a compositionally- and thermally-homogeneous mantle

Supporting Information:

Supporting Information may be found in the online version of this article.

Correspondence to:

C. Durán,
cecilia.duran@erdw.ethz.ch

Citation:

Durán, C., Khan, A., Ceylan, S., Charalambous, C., Kim, D., Drilleau, M., et al. (2022). Observation of a core-diffracted P-wave from a farside impact with implications for the lower-mantle structure of Mars. *Geophysical Research Letters*, *49*, e2022GL100887. https://doi.org/10.1029/2022GL100887

Received 19 AUG 2022
Accepted 26 OCT 2022

Author Contributions:

Conceptualization: C. Durán, A. Khan
Data curation: C. Durán, A. Khan, S. Ceylan, C. Charalambous, D. Kim
Formal analysis: C. Durán, A. Khan, S. Ceylan, D. Giardini
Methodology: C. Durán, A. Khan, S. Ceylan, C. Charalambous
Project Administration: D. Giardini
Software: C. Durán, A. Khan, S. Ceylan
Supervision: A. Khan, D. Giardini
Validation: C. Charalambous, M. Drilleau, H. Samuel
Visualization: C. Durán
Writing – original draft: C. Durán, A. Khan

Abstract We report on the observation of a diffracted P-wave (Pdiff) along the core of Mars from a distant impact that has been recorded by the Interior Exploration using Seismic Investigations, Geodesy and Heat Transport (InSight) mission. The identification of Pdiff allows us to sample the P-wave velocity structure of the lower mantle that hitherto could not be constrained because of lack of lower-mantle-traversing P-waves. In addition to Pdiff, we are able to pick PP-, PPP-, and SS-wave arrivals and locate the event to the farside of Mars in the vicinity of Tharsis, in agreement with the imaged location of the impact. This indicates that our joint single-station seismic event-location and structure-inversion scheme is both robust and accurate. Based on inversion of the body-wave arrival time picks made here, we find lower P-wave velocities in the deep mantle relative to predictions based on thermochemically homogeneous models.

Plain Language Summary Since the landing of the Interior Exploration using Seismic Investigations, Geodesy and Heat Transport (InSight) mission on Mars, ground vibration measurements emanating from marsquakes have revealed a large part of the interior structure of the planet. In this study, we analyze a new seismic event that at first glance differs from previous marsquakes because of its impact nature and farside location. For the first time, we observe a seismic phase that traverses the lower mantle of Mars, allowing us to constrain the seismic velocity structure from the surface to the core-mantle-boundary.

1. Introduction

Since its deployment, the SEIS (Seismic Experiment for Interior Structure) instrument (Lognonné et al., 2019) as part of the InSight (Interior Exploration using Seismic Investigations, Geodesy and Heat Transport) lander has been passively recording marsquakes (Banerdt et al., 2020) for over 1300 Sols (a Sol is a Martian day and corresponds to ∼24 hr 40 min) since landing, including ∼90 marsquakes at teleseismic distances with moment magnitudes (M_w) in the range 2.5–4.2 (Ceylan et al., 2022; Clinton et al., 2021; InSight Marsquake Service, 2022). The analysis of marsquakes has resulted in a significant improvement in our understanding of Martian seismicity (Giardini et al., 2020) and interior structure (Lognonné et al., 2020), including crustal and lithospheric thickness, crustal and mantle velocity structure, and core size and mean density (Drilleau et al., 2022; Durán et al., 2022; Khan et al., 2021, 2022; Kim, Lekić, et al., 2021; Kim et al., 2022; Knapmeyer-Endrun et al., 2021; Stähler et al., 2021). Yet, because of the absence of P-waves that have traversed the lower mantle (below ∼800 km depth), the deep mantle P-wave velocity structure remains unconstrained. In contrast, the detection of core-reflected S-waves (Durán et al., 2022; Stähler et al., 2021) helped constrain the S-wave velocity profiles down to the core-mantle-boundary (CMB).

To determine lower mantle P-wave velocity structure, we consider a recent event that occurred on Sol 1000 with one of the highest signal-to-noise ratios (SNRs) observed thus far (Sol 1189) by InSight (Horleston et al., 2022; InSight Marsquake Service, 2022). This second-most distant event has been matched with an impact on the surface of Mars at an epicentral distance and back-azimuth of ∼126° and 34.5°, respectively (Posiolova et al., 2022). The event occurred in Tempe Terra to the East of the Tharsis rise and North of Valles Marineris. Because of the farside location, S1000a (marsquakes are labeled by mission Sol of occurrence and sub-labeled alphabetically for Sols with more than one event) provides a unique opportunity to study the deep structure of Mars. Here,

Writing – review & editing: C. Durán, A. Khan, S. Ceylan, D. Kim, M. Drilleau, H. Samuel, D. Giardini

we provide an in-depth analysis of S1000a with the aim of presenting the first observation of a core-diffracted P-wave (hereinafter labeled Pdiff).

We first provide an overview of the event, after which we apply a number of processing steps to the waveform data that have been developed specifically for the purpose of detecting seismic body wave arrivals in the relatively strong scattering coda of marsquakes (Durán et al., 2022; Khan et al., 2021). Application of these methods to S1000a allows us to pick the main P- and S-wave arrivals (PP and SS) and the lower mantle traversing seismic phase Pdiff. Finally, we perform an inversion of the phases picked here with the body-wave travel time data set of Durán et al. (2022) to obtain improved models of Mars's P-wave velocity structure and test the capabilities of our joint seismic event-location and structure-inversion scheme on the basis of a known event location.

2. Event Overview

The Mars-calibrated moment magnitude M_w for event S1000a (Böse et al., 2021) is 4.1 ± 0.2 and one of the largest marsquakes to have been recorded to date. An overview of the event is shown in Figure 1. A scalogram of the event, computed as the absolute value of the continuous wavelet transform of the signal, is shown in Figure 1a and illustrates the temporal change in signal frequency content. As described in Horleston et al. (2022), and following the classification of Clinton et al. (2021), this event is a broadband event because of its frequency content ranging from 10 s to over 5 Hz (Figure 1a).

Low-frequency band-pass filtered (0.1–0.8 Hz) three-component waveforms in the vertical-radial-transverse system and their envelopes are shown in Figure 1b. Glitches, which are easily discernible in the scalogram as energy spikes that are mainly present at long periods, are masked in the waveforms to avoid misinterpretation. The filtered waveforms exhibit two main arrivals that, based on the differential travel time, are designated as the surface-reflected PP and SS body waves. The phase arrivals and the initial uncertainty on the picks assigned by the MarsQuake Service (MQS) are represented by vertical lines and orange bars, respectively. As shown in Figure 1b, the PP-wave energy can be clearly identified in the time-domain waveforms, while the SS-wave arrival is emergent, making the identification of the onset more difficult. Also visible on the vertical-component waveform is an additional arrival preceding PP, indicated by a vertical dashed line. A zoom-in of the vertical and radial components around this arrival is shown in Figures 1c and 1d. This phase was initially labeled as a P-wave that diffracts along the core-mantle boundary by Horleston et al. (2022) based on travel time predictions. In line with expectations for a steeply-arriving phase, the *Z*/*R* amplitude ratio for Pdiff is found to be larger than for the PP phase. This is also observed with synthetic waveforms (Figure S1 in Supporting Information S1).

3. Seismic Data Analysis

3.1. PP and SS

A zoom into the band-pass-filtered waveforms and their time-domain envelopes is shown in Figures 2a and 2d for time windows containing the early part of the PP- and SS-wave arrivals, respectively. Synthetic waveform simulations computed for an inclined force supports the presence of an SS-wave arrival on the transverse component (for details see Section S2 in Supporting Information S1). Consequently, vertical- and transverse-component traces are shown for PP- and SS-wave arrivals, respectively. Because they visually enhance the arrival of energy packages, envelopes are important for the identification of seismic phases in the low-magnitude noisy marsquake signals recorded so far (Durán et al., 2022; Khan et al., 2021).

As body waves are characterized by linear polarization (Haubrich et al., 1963; Tanimoto et al., 2006), we apply a time-domain polarization method to increase the SNR of the linearly-polarized part of the signal through principal component analysis (Montalbetti & Kanasewich, 1970). Filtered polarized vertical- and transverse-component traces and their time-domain envelopes for S1000a are shown in Figures 2b and 2E. These polarized traces, in comparison to the waveforms shown in Figures 2a and 2d, exhibit high-amplitude packages of energy associated with body waves.

A complementary approach that has proven helpful for the identification of seismic phases is the use of narrow-band-filtered time-domain waveform envelopes (filter banks) (Durán et al., 2022; Khan et al., 2021). To this end, we filter the velocity traces in frequency bands half an octave wide around a central frequency that ranges from 1/5 to 1 Hz, comprising the low-frequency energy of the signal, and compute their envelopes. To avoid interference from non-seismic signals, we ensure that the filter banks are devoid of glitch-, donk-, or

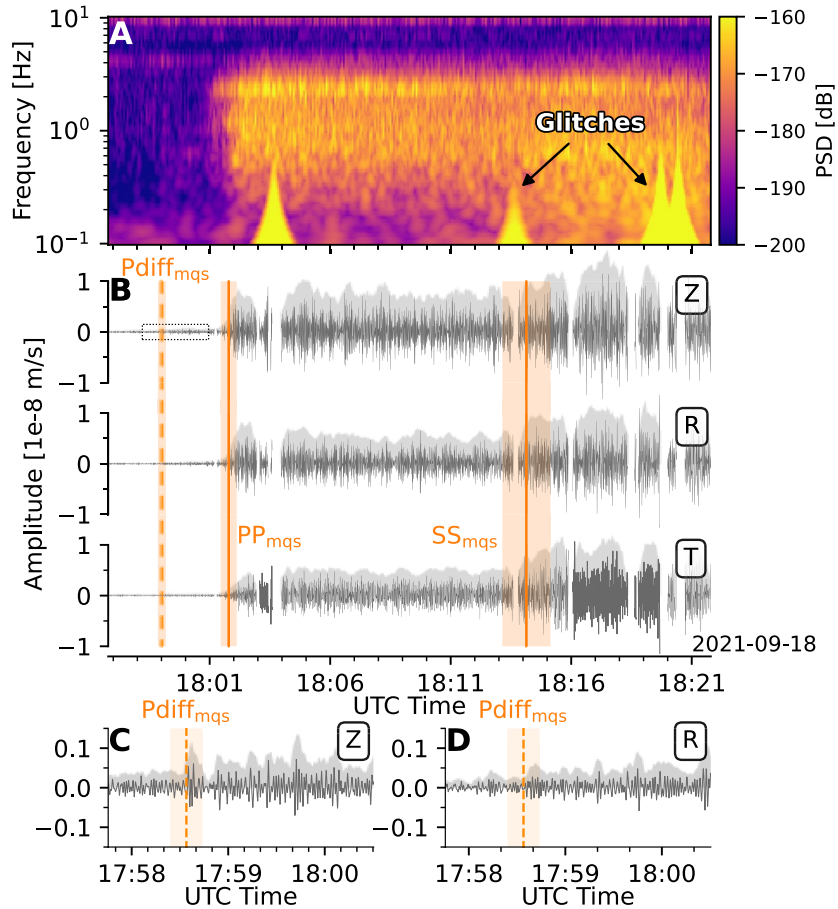

Figure 1. Three-component scalogram (a), band-pass filtered traces (0.1–0.8 Hz) and their time-domain envelopes (b) for the vertical (*Z*), radial (*R*), and transverse (*T*) component waveforms of event S1000a, and zoom-in around the Pdiff arrival (c and d) for the *Z* and *R* components. Time-domain envelopes are shown in light gray, while filtered traces are shown in dark gray. Seismic phase picks by the MarsQuake Service (InSight Marsquake Service, 2022) and uncertainties are shown as orange vertical lines and vertical bars, respectively. The scalogram is built as the sum of the squared scalograms of each component (see single-component scalograms in Figure S2 in Supporting Information S1). Waveforms are masked where glitches occurred to avoid misinterpretation of phases. Envelopes are computed for 5-s long time windows. Waveforms spanning longer time series are shown in Figure S3 in Supporting Information S1.

atmospheric-related artifacts (Kim, Davis, et al., 2021). Envelopes for all filters considered here are shown in Figures 2c and 2f. The onset of increase in energy is observed in the envelopes for most of the frequencies that coincides with that observed for the polarized waveforms in Figures 2b and 2e as indicated by the vertical orange bars across panels a–c and d–f for the PP- and SS-wave arrivals, respectively.

Based on previous identification of body-wave arrivals, we rely on the criteria detailed in Durán et al. (2022) for an arrival to qualify as a seismic phase: (a) arrivals should be present across different frequency bands; (b) arrivals should be present in both, non-polarized and polarized traces/envelopes; and (c) arrivals have to follow a certain sequence (e.g., differential travel time between PPP and PP has to be less than that between PP and P). Following this procedure, we select the arrivals that are represented by vertical orange dotted lines in Figure 2 as our PP- and SS-wave picks. Uncertainties, which are assigned based on the energy onset observed across the different techniques, and typically range between 1 and 10 s, are indicated by orange bars.

3.2. Pdiff

To enhance the Pdiff signal and refine the initial MQS Pdiff pick of Horleston et al. (2022), we band-pass filter the traces in the frequency range 0.2–0.6 Hz and show vertical-component waveform and its time-domain envelope in Figure 2g. At and following the expected location of the Pdiff arrival, signal energy increases and

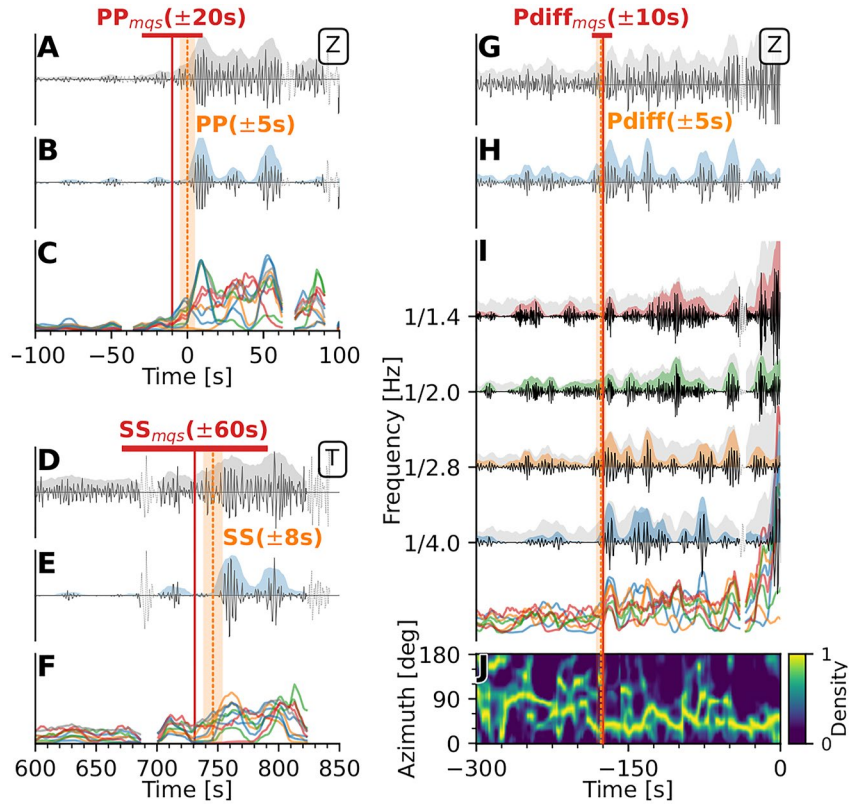

Figure 2. Seismic waveform analysis and phase picks for event S1000a. Analysis of PP (vertical component, a–c), SS (transverse component, d–f), and Pdiff (vertical component, g–j). Panels (a, d, g) show the band-pass filtered waveforms (black) and their envelopes (gray). Panels (b, e, h) show the band-pass filtered polarized waveforms (black) and their envelopes (blue). Panels (c and f) show all time-domain envelopes across the different frequency bands (see Figure S8 in Supporting Information S1). Panel (i) shows traces (black lines) and their time-domain envelopes (color) across different frequency bands (filter banks) for the polarized waveforms, and envelopes (gray) for non-polarized waveforms. All envelopes across the various filter banks are overlapped at the bottom. Panel (j) shows the temporal change in azimuthal density in the 0.2–0.6 Hz frequency band (see Figure S6 in Supporting Information S1 for extended version including PP). Azimuth is constrained to lie in the 0°–180° range, with a 180° ambiguity. Initial seismic phase picks by the MarsQuake Service and uncertainties on arrival picks (InSight Marsquake Service, 2022) are represented by the vertical red solid lines and horizontal red bars, respectively. Our phase picks, including uncertainties, are indicated by the orange vertical dotted lines and bars, respectively. Amplitudes of traces and envelopes are normalized by their maxima and scaled for better visualization. Waveforms and envelopes are masked where glitches occurred to avoid misinterpretation of phases. Time is relative to arrival of the PP-wave onset selected in this study in the time-domain waveforms (see Table S1 in Supporting Information S1). An extended version of the figure that includes the PP arrival is shown in Supporting Information S1.

is maintained above that present before the arrival, in agreement with waveform modeling results (Figure S1 in Supporting Information S1).

Subsequently, we apply a time-domain polarization filter as described in the previous section to increase the SNR of linearly-polarized signals. The polarized waveforms and their envelopes are shown in Figure 2h, and exhibit arrival of an energy package at the location of the MQS Pdiff arrival. Comparison of the time-domain non-polarised (gray, Figure 2g) and polarised (blue, Figure 2h) envelopes indicates a diminution of the polarized signals preceding the Pdiff arrival and are therefore likely to be related to elliptically-polarized noise.

To better visualize the characteristics of the Pdiff arrival, we filter polarized and non-polarized waveforms in narrow frequency bands. The filter banks are shown in Figure 2i and allow for improved identification of the onset of Pdiff across different frequency bands. While Pdiff is relatively strong at lower frequencies (1/2.8 and 1/4 Hz), it is nevertheless also observable at higher frequencies. This is supported by synthetic waveform modeling that indicates that the amplitude decrease with distance is less pronounced at the frequencies employed here (see Section S3 in Supporting Information S1 for details), which is unlike what is observed for Pdiff on

Earth (e.g., Hosseini & Sigloch, 2015). In line with our aforementioned criteria for energy arrivals to qualify as seismic phases, the only signal that is present across all frequency bands is the phase indicated by a vertical red line in Figure 2i. All envelopes for both polarized and non-polarized waveforms are overlapped at the bottom of Figure 2i and show an increase in signal energy after arrival of the phase relative to what is present before. Consequently, we consider the selected phase to be Pdiff. Although core-diffracted P-wave on Earth are dispersive (Hosseini & Sigloch, 2015), this is not observed in the present data and is probably due to the limited frequency range over which this phase can be observed relative to what is observed on Earth (∼2 to 30 s).

To validate the selected phase, we verify that its azimuth is consistent with that of the PP-wave arrival. For this, we apply a polarization analysis to infer the instantaneous back-azimuth of the three-component seismic data (see Section S4 in Supporting Information S1 for details).

To represent changes in azimuth with arrival of seismic phases, we compute normalized azimuthal probability density curves in the frequency band (0.2–0.6 Hz) considering 5-s long time windows. This is shown in Figure 2j. To avoid a large spread of azimuths due to changes in particle motion for signals arriving from the same direction (e.g., because of surface reflections), we consider azimuths between 0° and 180°. In the ∼125 s prior to the arrival of the Pdiff phase (dotted vertical lines), azimuth is generally unstable. However, following Pdiff and until the end of the time window, the azimuth exhibits a consistent polarization with a direction centered around 30° with respect to North (±180°). This estimation agrees with the azimuth observed for the PP-wave arrival (see Figure S6 in Supporting Information S1), indicating, as expected, that Pdiff and PP exhibit the same particle motion (±180°). The fact that the arrival of Pdiff is characterized by an overall change in polarization with respect to the dominant azimuth of earlier arriving phases, supports the selection of our pick and its uncertainty.

To exclude the possibility of a wind-induced signal, which is one of the main sources of noise in the InSight seismic data given the ubiquity of wind on Mars even during the quietest periods of the day (Banfield et al., 2020), we apply comodulation analysis to Pdiff (Charalambous et al., 2021). This technique partitions the signal into seismic and environmental contributions and is critical for assessing the contribution of wind-induced noise to low-amplitude seismic phases. The analysis (see Section S5 in Supporting Information S1 for details) shows that our Pdiff pick is unlikely to be contaminated by signals originating in the atmosphere.

Our final body-wave picks selected at the onset of energy of the corresponding phases, including a PPP-wave arrival described in Section S6 in Supporting Information S1, are listed in Table S1 in Supporting Information S1. For completeness, we also include the MQS PP, SS, and Pdiff picks. Finally, we looked for Sdiff, but were unable to positively identify this phase, because of the interference of other phases and spurious signal (see Figure S9 in Supporting Information S1).

4. Inversion

To invert for models of interior structure, we follow the method laid out in our previous work (Durán et al., 2022; Khan et al., 2021) and consider a seismic and a geophysical parameterization, which is based on mineral physics data. As described in detail in Sections S7 and S8 in Supporting Information S1, we consider a spherically symmetric model of Mars, divided into three regions comprising crust, mantle, and core that are further subdivided in a number of layers each parameterized using either P- and S-wave velocities (seismic parameterization) or thermo-chemical parameters (mineral physics parameterization). For the inversion presented here, we fix the epicentral distance of S1000a according to the observed location of the surface impact (Posiolova et al., 2022), yet for the purpose of verifying our location algorithm, we also perform an inversion with variable location. We invert the body-wave picks made in this study with those from our earlier analysis (Durán et al., 2022). The inverse problem of determining seismic velocity profiles is solved using the probabilistic approach of Mosegaard and Tarantola (1995).

5. Results and Discussion

Inverted velocity profiles, differential travel time misfits for S1000a, ray path geometry, and event locations are shown in Figure 3 (for misfits and epicentral distance distributions of all the other events, see Figures S11 and S12 in Supporting Information S1). All differential travel times are fit with the exception of $T_{\mathrm{Pdiff}} - T_{\mathrm{PP}}$ for the

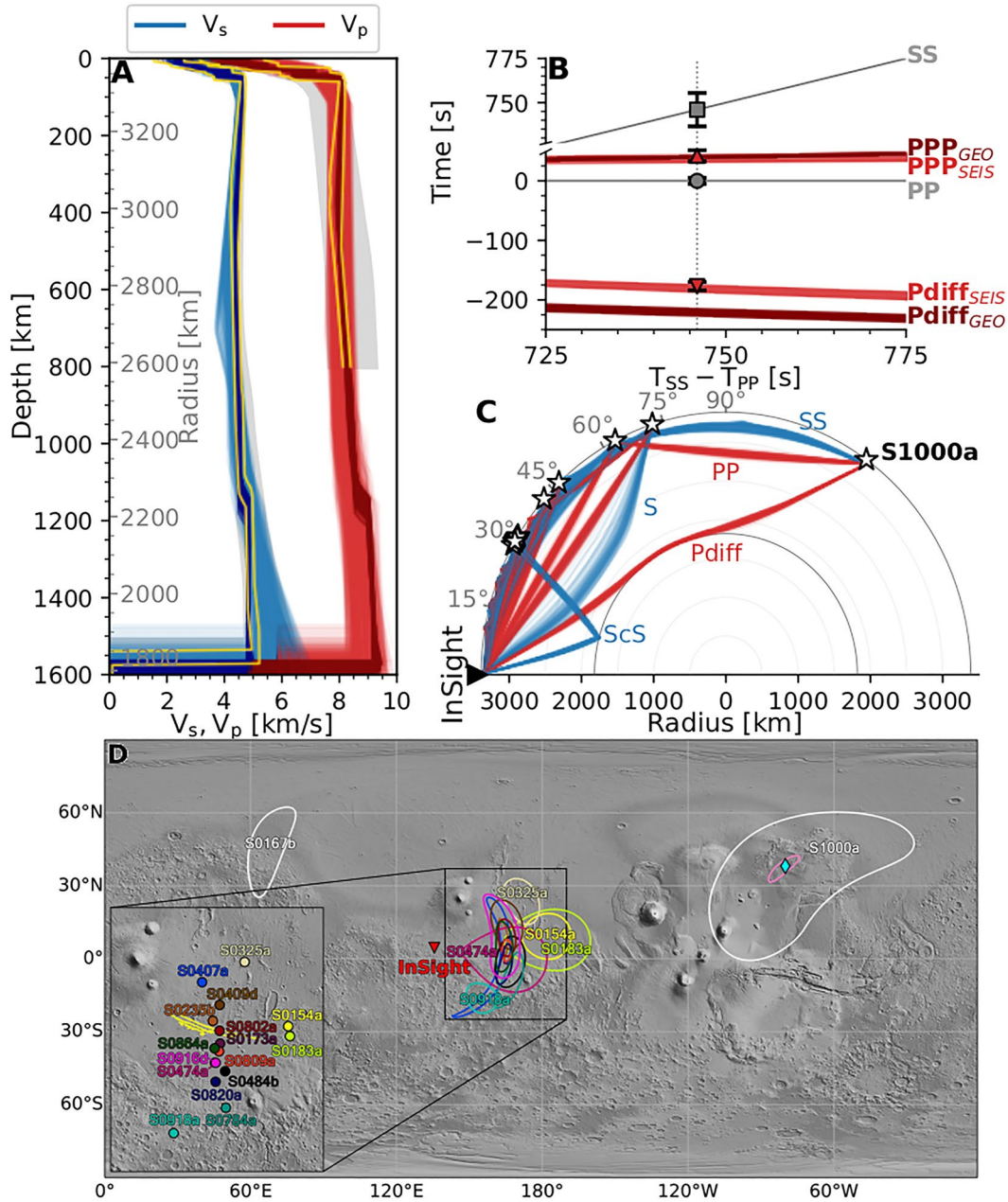

Figure 3. (a) Inverted seismic P- and S-wave velocity profiles based on the seismic (light blue and red lines) and geophysical (dark blue and red lines) parameterization. For comparison, light gray (seismic parameterization) and yellow (geophysical parameterization) lines show the results of Durán et al. (2022). (b) Computed differential travel time misfits for S1000a. The body-wave phase picks are aligned by their observed $T_{SS} - T_{PP}$ time. Markers and error bars represent observed differential travel times and their uncertainty, respectively. Colored bands represent predictions of differential travel times based on the inverted seismic (SEIS) and geophysical (GEO) models. (c) Body-wave ray path geometry for all low-frequency events and phases considered in the inversion, computed using the seismic models. Events are indicated by stars. All P- and S-wave-related paths are shown in red and blue, respectively. (d) Martian seismicity location map based on the Mars Orbiter Laser Altimeter surface relief map (Smith et al., 2001). The ellipses describe the estimated locations, including uncertainty of major low-frequency marsquakes. The imaged impact location for S1000a is indicated by a cyan diamond, whereas the pink and white ellipses show the locations determined in this study and by the MarsQuake Service (InSight Marsquake Service, 2022), respectively. The back-azimuth determined here is obtained from the azimuthal density plot (Figure S6C in Supporting Information S1) by considering the mean and spread in azimuth over a 100-s time window around the PP-wave arrival. The inset shows a zoom-in of the low-frequency family events that are clustered in the Cerberus Fossae region and represent the "best" locations. A single event (S0167b) is indicated by a white ellipse NW of InSight.

geophysical parameterization (Figure 3b), which will be discussed further below. The location of the events considered here are shown in Figure 3c, which also illustrates the ray path geometry based on the inverted velocity models and source-receiver configuration.

The inverted velocity profiles shown in Figure 3a are for the case of a fixed impact location for S1000a (the inverted velocity profiles for the variable-location inversion are shown in Figure S10 in Supporting Information S1 and are considered below). Comparing the two parameterizations indicates that the seismic parameterization is more flexible as reflected in an increase in sampling width relative to the mineral-physics-informed parameterization. Comparison between the new and our previously-obtained velocity structure from Durán et al. (2022) shows that (a) we now constrain P-wave velocity structure between 800 km depth and the CMB; (b) the range of sampled upper-mantle P-wave velocity profiles based on the seismic parameterization is narrower in comparison to earlier models (compare gray and light red bands); (c) an earlier suggestion of a slightly negative upper-mantle P-wave velocity gradient appears to be confirmed (previously not seen in the seismic parameterization as indicated by the gray bands), which is evidence in support of a strong thermal gradient across the lithosphere as reported earlier (Durán et al., 2022; Khan et al., 2021); and (d) P-wave velocities in the deep mantle (below 800 km depth) based on the seismic parameterization are lower relative to those predicted by the geophysical parameterization (compare light and dark red bands). The latter observation is driven by Pdiff as indicated in the differential travel time misfit plot (Figure 3b), since Pdiff based on the geophysical parameterization arrives ~30 s early compared to our present pick. This suggests deviations in lower-mantle V_P/V_S ratio from current predictions based on the working assumption of a compositionally and thermally homogeneous mantle (cf., Section S7 in Supporting Information S1) as implied by geodynamic models that incorporate a partially molten zone above the CMB (Samuel et al., 2021). Lateral variations in crust and mantle structure could also affect the residual travel time, yet this is difficult to ascertain with a single station. To distinguish between these possibilities, additional data are required since Pdiff is currently the only seismic phase that constrains lower mantle P-wave velocity structure.

Finally, since the location of S1000a is known exactly, we can check the accuracy of our joint single-station seismic event-location and structure-inversion scheme described in Durán et al. (2022). To this end, we plotted our inverted location for S1000a based on the variable-location-inversion on a surface relief map of Mars (Figure 3d) together with the imaged location of the impact and the location determined by MQS (epicentral distances and back-azimuths are summarized in Table S1 in Supporting Information S1). Comparison between the various locations for S1000a shows that (a) relative to the MQS location (InSight Marsquake Service, 2022) (white ellipse), ours (pink ellipse) is better constrained as a result of improved body-wave picks and (b) our location is in good agreement with the known location of the impact (cyan diamond). The comparison illustrates that our joint scheme is performing optimally and that "pinpoint" location capabilities are achievable with a single-station and a suitable set of events/phase picks. For comparison, we also show the locations of other low-frequency family events from Zenhäusern et al. (2022). With the exception of a few events, most of the located tectonic marsquakes are centered on the Cerberus Fossae fault system (yellow lines oriented NW-SE in inset in Figure 3d) (Brinkman et al., 2021; Jacob et al., 2022), which consists of a series of major grabens that are between 250 and 600 km long (Perrin et al., 2022).

6. Conclusion

In this paper, we analyzed a particular event (S1000a), which happens to be not only one of the largest events observed to date, but also one of the furthest. Analysis of observed and synthetic seismic waveforms allowed us to identify a core-diffracted P-wave for the first time, in addition to the main arriving P- and S-wave energy in the form of PP- and SS-waves, including a PPP-wave arrival. Based on the picks, the event is found to be located on the farside of Mars at an epicentral distance of ~127° with a back-azimuth around 36° in close agreement with the observed impact location. On account of the observation of Pdiff and its ray-path geometry, we have been able to place constraints on lower mantle P-wave velocity structure between 800 km depth and the CMB that up until the present had remained unconstrained. We also showed that our joint seismic event-location and structure-inversion scheme based on seismic phase picks from a single station is functioning optimally in that it predicts a location for S1000a in excellent agreement with the imaged location.

Data Availability Statement

The InSight event catalog V11 (comprising all events, including phase picks until April 2022) and waveform data are available from the IRIS-DMC, NASA-PDS, SEIS-InSight data portal and IPGP data center (InSight Mars SEIS Data Service, 2019a; InSight Mars SEIS Data Service, 2019b; InSight Marsquake Service, 2022). Seismic waveforms are also available from the NASA PDS (National Aeronautics and Space Administration Planetary Data System) (InSight Mars SEIS Data Service, 2019a). The data were processed with ObsPy (Beyreuther et al., 2010), NumPy (Harris et al., 2020) and Scipy (Virtanen et al., 2020), and visualizations were created with Matplotlib (Hunter, 2007).

Acknowledgments

The authors are grateful to Jeroen Ritsema for a very constructive review that led to an improved manuscript. Comments by an anonymous reviewer were also appreciated as were those of Sanne Cottaar on an earlier version of this manuscript. Andrew Dombard is thanked for editorial handling. C.D., A.K., and D.G. would like to acknowledge support from ETH through the ETH+ funding scheme (ETH+02 19-1: "Planet Mars"). The authors acknowledge the NASA, CNES, partner agencies and institutions (UKSA, SSO, DLR, JPL, IPGP-CNRS, ETHZ, ICL, MPS-MPG), and the operators of JPL, SISMOC, MSDS, IRIS-DMC, and PDS for providing SEED SEIS data. Finally, the authors thank Géraldine Zenhäusern for providing us with the Martian seismicity location map. This is InSight contribution 269.

References

Banerdt, W. B., Smrekar, S. E., Banfield, D., Giardini, D., Golombek, M., Johnson, C. L., et al. (2020). Initial results from the InSight mission on Mars. *Nature Geoscience*, *13*(3), 183–189. https://doi.org/10.1038/s41561-020-0544-y

Banfield, D., Spiga, A., Newman, C., Forget, F., Lemmon, M., Lorenz, R., et al. (2020). The atmosphere of Mars as observed by InSight. *Nature Geoscience*, *13*(3), 190–198. https://doi.org/10.1038/s41561-020-0534-0

Beyreuther, M., Barsch, R., Krischer, L., Megies, T., Behr, Y., & Wassermann, J. (2010). ObsPy: A Python toolbox for seismology. *Seismological Research Letters*, *81*(3), 530–533. https://doi.org/10.1785/gssrl.81.3.530

Böse, M., Stähler, S. C., Deichmann, N., Giardini, D., Clinton, J., Lognonné, P., et al. (2021). Magnitude scales for marsquakes calibrated from InSight data. *Bulletin of the Seismological Society of America*, *111*(6), 3003–3015. https://doi.org/10.1785/0120210045

Brinkman, N., Stähler, S. C., Giardini, D., Schmelzbach, C., Khan, A., Jacob, A., et al. (2021). First focal mechanisms of marsquakes. *Journal of Geophysical Research: Planets*, *126*(4), e2020JE006546. https://doi.org/10.1029/2020JE006546

Ceylan, S., Clinton, J. F., Giardini, D., Stähler, S. C., Horleston, A., Kawamura, T., et al. (2022). The marsquake catalogue from insight, sols 0–1011. *Physics of the Earth and Planetary Interiors*, *333*, 106943. https://doi.org/10.1016/j.pepi.2022.106943

Charalambous, C., Stott, A. E., Pike, W. T., McClean, J. B., Warren, T., Spiga, A., et al. (2021). A comodulation analysis of atmospheric energy injection into the ground motion at InSight, Mars. *Journal of Geophysical Research: Planets*, *126*(4), e2020JE006538. https://doi.org/10.1029/2020JE006538

Clinton, J. F., Ceylan, S., van Driel, M., Giardini, D., Stähler, S. C., Böse, M., et al. (2021). The Marsquake catalogue from InSight, sols 0–478. *Physics of the Earth and Planetary Interiors*, *310*, 106595. https://doi.org/10.1016/j.pepi.2020.106595

Drilleau, M., Samuel, H., Garcia, R. F., Rivoldini, A., Perrin, C., Michaut, C., et al. (2022). Marsquake locations and 1-d seismic models for Mars from insight data. *Journal of Geophysical Research: Planets*, *127*(9), e2021JE007067. https://doi.org/10.1029/2021JE007067

Durán, C., Khan, A., Ceylan, S., Zenhäusern, G., Stähler, S., Clinton, J., & Giardini, D. (2022). Seismology on Mars: An analysis of direct, reflected, and converted seismic body waves with implications for interior structure. *Physics of the Earth and Planetary Interiors*, *325*, 106851. https://doi.org/10.1016/j.pepi.2022.106851

Giardini, D., Lognonné, P., Banerdt, W. B., Pike, W. T., Christensen, U., Ceylan, S., et al. (2020). The seismicity of Mars. *Nature Geoscience*, *13*(3), 205–212. https://doi.org/10.1038/s41561-020-0539-8

Harris, C. R., Millman, K. J., van der Walt, S. J., Gommers, R., Virtanen, P., Cournapeau, D., et al. (2020). Array programming with NumPy. *Nature*, *585*(7825), 357–362. https://doi.org/10.1038/s41586-020-2649-2

Haubrich, R., Munk, W., & Snodgrass, F. (1963). Comparative spectra of microseisms and swell. *Bulletin of the Seismological Society of America*, *53*(1), 27–37. https://doi.org/10.1785/bssa0530010027

Horleston, A. C., Clinton, J. F., Ceylan, S., Giardini, D., Charalambous, C., Irving, J. C. E., et al. (2022). The far side of Mars: Two distant marsquakes detected by InSight. *The Seismic Record*, *2*(2), 88–99. https://doi.org/10.1785/0320220007

Hosseini, K., & Sigloch, K. (2015). Multifrequency measurements of core-diffracted *P* waves (Pdiff) for global waveform tomography. *Geophysical Journal International*, *203*(1), 506–521. https://doi.org/10.1093/gji/ggv298

Hunter, J. D. (2007). Matplotlib: A 2D graphics environment. *Computing in Science & Engineering*, *9*(3), 90–95. https://doi.org/10.1109/MCSE.2007.55

InSight Marsquake Service. (2022). *Mars seismic catalogue, InSight mission; V11 2022-07-01*. ETHZ, IPGP, JPL, ICL, Univ. Bristol. https://doi.org/10.12686/a17

InSight Mars SEIS Data Service. (2019a). InSight SEIS data bundle. PDS Geosciences (GEO) Node. https://doi.org/10.17189/1517570

InSight Mars SEIS Data Service. (2019b). SEIS raw data, Insight Mission. IPGP, JPL, CNES, ETHZ, ICL, MPS, ISAE-Supaero, LPG, MFSC. https://doi.org/10.18715/SEIS.INSIGHT.XB_2016

Jacob, A., Plasman, M., Perrin, C., Fuji, N., Lognonné, P., Xu, Z., et al. (2022). Seismic sources of InSight marsquakes and seismotectonic context of Elysium Planitia, Mars. *Tectonophysics*, *837*, 229434. https://doi.org/10.1016/j.tecto.2022.229434

Khan, A., Ceylan, S., van Driel, M., Giardini, D., Lognonné, P., Samuel, H., et al. (2021). Upper mantle structure of Mars from InSight seismic data. *Science*, *373*(6553), 434–438. https://doi.org/10.1126/science.abf2966

Khan, A., Liebske, C., Rozel, A., Rivoldini, A., Nimmo, F., Connolly, J. A. D., et al. (2018). A geophysical perspective on the bulk composition of Mars. *Journal of Geophysical Research: Planets*, *123*(2), 575–611. https://doi.org/10.1002/2017JE005371

Khan, A., Sossi, P., Liebske, C., Rivoldini, A., & Giardini, D. (2022). Geophysical and cosmochemical evidence for a volatile-rich Mars. *Earth and Planetary Science Letters*, *578*, 117330. https://doi.org/10.1016/j.epsl.2021.117330

Kim, D., Banerdt, W. B., Ceylan, S., Giardini, D., Lekić, V., Lognonné, P., et al. (2022). Surface waves and crustal structure on Mars. *Science*, *378*(6618), 417–421. https://doi.org/10.1126/science.abq7157

Kim, D., Davis, P., Lekić, V., Maguire, R., Compaire, N., Schimmel, M., et al. (2021). Potential pitfalls in the analysis and structural interpretation of seismic data from the Mars InSight mission. *Bulletin of the Seismological Society of America*, *111*(6), 2982–3002. https://doi.org/10.1785/0120210123

Kim, D., Lekić, V., Irving, J. C. E., Schmerr, N., Knapmeyer-Endrun, B., Joshi, R., et al. (2021). Improving constraints on planetary Interiors with PPs receiver functions. *Journal of Geophysical Research: Planets*, *126*(11). https://doi.org/10.1029/2021je006983

Knapmeyer-Endrun, B., Panning, M. P., Bissig, F., Joshi, R., Khan, A., Kim, D., et al. (2021). Thickness and structure of the Martian crust from InSight seismic data. *Science*, *373*(6553), 438–443. https://doi.org/10.1126/science.abf8966

Lognonné, P., Banerdt, W., Pike, W., Giardini, D., Christensen, U., Garcia, R., et al. (2020). Constraints on the shallow elastic and anelastic structure of Mars from InSight seismic data. *Nature Geoscience*, *13*(3), 213–220. https://doi.org/10.1038/s41561-020-0536-y

Lognonné, P., Banerdt, W. B., Giardini, D., Pike, W., Christensen, U., Laudet, P., et al. (2019). SEIS: Insight's seismic experiment for internal structure of Mars. *Space Science Reviews*, *215*(1), 12. https://doi.org/10.1007/s11214-018-0574-6

Montalbetti, J. F., & Kanasewich, E. R. (1970). Enhancement of teleseismic body phases with a polarization filter. *Geophysical Journal International*, *21*(2), 119–129. https://doi.org/10.1111/j.1365-246X.1970.tb01771.x

Mosegaard, K., & Tarantola, A. (1995). Monte Carlo sampling of solutions to inverse problems. *Journal of Geophysical Research*, *100*(B7), 12431–12447. https://doi.org/10.1029/94jb03097

Perrin, C., Jacob, A., Lucas, A., Myhill, R., Hauber, E., Batov, A., et al. (2022). Geometry and segmentation of Cerberus Fossae, Mars: Implications for marsquake properties. *Journal of Geophysical Research: Planets*, *127*(1), e2021JE007118. https://doi.org/10.1029/2021JE007118

Posiolova, L. V., Lognonné, P., Banerdt, W. B., Clinton, J., Collins, G. S., Kawamura, T., et al. (2022). Largest recent impact craters on Mars: Orbital imaging and surface seismic co-investigation. *Science*, *378*(6618), 412–417. https://doi.org/10.1126/science.abq7704

Samuel, H., Ballmer, M. D., Padovan, S., Tosi, N., Rivoldini, A., & Plesa, A.-C. (2021). The thermo-chemical evolution of Mars with a strongly stratified mantle. *Journal of Geophysical Research: Planets*, *126*(4), e2020JE006613. https://doi.org/10.1029/2020JE006613

Smith, D. E., Zuber, M. T., Frey, H. V., Garvin, J. B., Head, J. W., Muhleman, D. O., et al. (2001). Mars Orbiter Laser Altimeter: Experiment summary after the first year of global mapping of Mars. *Journal of Geophysical Research*, *106*(E10), 23689–23722. https://doi.org/10.1029/2000JE001364

Stähler, S. C., Khan, A., Banerdt, W. B., Lognonné, P., Giardini, D., Ceylan, S., et al. (2021). Seismic detection of the Martian core. *Science*, *373*(6553), 443–448. https://doi.org/10.1126/science.abi7730

Tanimoto, T., Ishimaru, S., & Alvizuri, C. (2006). Seasonality in particle motion of microseisms. *Geophysical Journal International*, *166*(1), 253–266. https://doi.org/10.1111/j.1365-246x.2006.02931.x

Virtanen, P., Gommers, R., Oliphant, T. E., Haberland, M., Reddy, T., Cournapeau, D., et al. (2020). SciPy 1.0: Fundamental algorithms for scientific computing in Python. *Nature Methods*, *17*(3), 261–272. https://doi.org/10.1038/s41592-019-0686-2

Zenhäusern, G., Stähler, S. C., Clinton, J. F., Giardini, D., Ceylan, S., & Garcia, R. F. (2022). Low-frequency marsquakes and where to find them: Back azimuth determination using a polarization analysis approach. *Bulletin of the Seismological Society of America*, *112*(4), 1787–1805. https://doi.org/10.1785/0120220019

References From the Supporting Information

Ceylan, S., Clinton, J. F., Giardini, D., Böse, M., Charalambous, C., van Driel, M., et al. (2021). Companion guide to the marsquake catalog from InSight, Sols 0–478: Data content and non-seismic events. *Physics of the Earth and Planetary Interiors*, *310*, 106597. https://doi.org/10.1016/j.pepi.2020.106597

Connolly, J. A. D. (2009). The geodynamic equation of state: What and how. *Geochemistry, Geophysics, Geosystems*, *10*(10), Q10014. https://doi.org/10.1029/2009GC002540

Dahmen, N. L., Zenhäusern, G., Clinton, J. F., Giardini, D., Stähler, S. C., Ceylan, S., et al. (2021). Resonances and Lander Modes Observed by InSight on Mars (1–9 Hz). *Bulletin of the Seismological Society of America*, *111*(6), 2924–2950. https://doi.org/10.1785/0120210056

Kristeková, M., Kristek, J., & Moczo, P. (2009). Time-frequency misfit and goodness-of-fit criteria for quantitative comparison of time signals. *Geophysical Journal International*, *178*(2), 813–825. https://doi.org/10.1111/j.1365-246x.2009.04177.x

Nissen-Meyer, T., van Driel, M., Stähler, S. C., Hosseini, K., Hempel, S., Auer, L., et al. (2014). AxiSEM: Broadband 3-D seismic wavefields in axisymmetric media. *Solid Earth*, *5*(1), 425–445. https://doi.org/10.5194/se-5-425-2014

Rivoldini, A., Van Hoolst, T., Verhoeven, O., Mocquet, A., & Dehant, V. (2011). Geodesy constraints on the interior structure and composition of Mars. *Icarus*, *213*(2), 451–472. https://doi.org/10.1016/j.icarus.2011.03.024

Sacks, S. I. (1966). Diffracted wave studies of the Earth's core: 1. Amplitudes, core size, and rigidity. *Journal of Geophysical Research*, *71*(4), 1173–1181. https://doi.org/10.1029/jz071i004p01173

Schimmel, M., & Gallart, J. (2003). The use of instantaneous polarization attributes for seismic signal detection and image enhancement. *Geophysical Journal International*, *155*(2), 653–668. https://doi.org/10.1046/j.1365-246x.2003.02077.x

Schimmel, M., Stutzmann, E., Ardhuin, F., & Gallart, J. (2011). Polarized Earth's ambient microseismic noise. *Geochemistry, Geophysics, Geosystems*, *12*(7), Q07014. https://doi.org/10.1029/2011gc003661

Stixrude, L., & Lithgow-Bertelloni, C. (2005). Thermodynamics of mantle minerals – I. Physical properties. *Geophysical Journal International*, *162*(2), 610–632. https://doi.org/10.1111/j.1365-246X.2005.02642.x

Stixrude, L., & Lithgow-Bertelloni, C. (2011). Thermodynamics of mantle minerals – II. Phase equilibria. *Geophysical Journal International*, *184*(3), 1180–1213. https://doi.org/10.1111/j.1365-246X.2010.04890.x